Interfacial structure and magnetic coupling at Fe_3O_4/FeO (001) and (111) interfaces

Ziyi Sun,[1,2,*] Shanshan Chen,[1,2,*] Yixiao Jiang,[1,2,†] Tingting Yao,[1,2,‡] Chunyang Gao,[1,2] Chunlin Chen,[1,2] Xiu-Liang Ma,[3,4,5] and Hengqiang Ye[6]

[1]*Shenyang National Laboratory for Materials Science, Institute of Metal Research, Chinese Academy of Sciences, Shenyang 110016, China*
[2]*School of Materials Science and Engineering, University of Science and Technology of China, Shenyang 110016, China*
[3]*Bay Area Center for Electron Microscopy, Songshan Lake Materials Laboratory, Dongguan 523808, China*
[4]*Institute of Physics, Chinese Academy of Sciences, Beijing 100190, China*
[5]*Lanzhou University of Technology, School of Materials Science and Engineering, Lanzhou 730050, China*
[6]*Ji Hua Laboratory, Foshan 528200, China*

(Received 14 August 2023; revised 8 January 2024; accepted 12 February 2024; published 6 March 2024)

Heterointerfaces between ferromagnetic and antiferromagnetic materials play an important role in the development and applications of magnetic and electronic devices. Here, atomic and electronic structures of two types of Fe_3O_4/FeO interfaces with different magnetic coupling modes have been investigated by combining advanced transmission electron microscopy and first-principles calculations. It is found that the Fe_3O_4/FeO (001) and Fe_3O_4/FeO (111) interfaces can be formed between FeO and Fe_3O_4 due to different phase transformations. The Fe_3O_4/FeO (111) interface is generally closer to the steady state. The electronic structure of both types of Fe_3O_4/FeO interfaces changes significantly, which leads to a metal-insulator transition of the Fe_3O_4 layer at the interfaces. The energy difference between the ferromagnetic and antiferromagnetic coupling states across the Fe_3O_4/FeO interfaces is very small, indicating that magnetic flip-flopping easily occurs in the Fe_3O_4/FeO system. The atomic magnetic moment of the interfacial Fe atoms at the Fe_3O_4/FeO (001) interface decreases by ~10% due to the preferentially occupied d_{xz} and d_{yz} orbitals, while that at the Fe_3O_4/FeO (111) interface remains almost unchanged. These findings suggest that the Fe_3O_4/FeO interfaces are susceptible to magnetic coupling transition and may find applications in low-power consumption magnetic and electronic devices.

DOI: 10.1103/PhysRevB.109.094405

I. INTRODUCTION

Ferromagnetic (FM) materials are widely used in the field of magnetic recording and storage [1–5]. With the explosive data growth, the energy consumption for information recording and storage increases rapidly, which is partly due to the ineffective Joule heat of the current for the generation of magnetic field. In addition, magnetic memory devices based on FM materials are easily disturbed by the surrounding stray magnetic field, thereby resulting in "demagnetization" and data loss [6]. To increase the stability of magnetic storage information, ferromagnetic/antiferromagnetic (FM/AFM) systems have become the popular design for high-density recording media since AFM materials have an exchange bias effect on the pinned FM materials [5,7,8].

It is generally accepted that the exchange bias effect is macroscopically manifested as the shift of the hysteresis line with respect to the zero field, and microscopically the exchange bias originates from the exchange coupling of the uncompensated magnetic moments at the interface [5,9–12]. This effect has been widely used in a variety of magnetoelectric devices, such as readout heads of computers and various magnetic sensors [13], but the intrinsic mechanism has not been completely revealed so far. Therefore, the FM/AFM interface effect should be approached from a more microscopic perspective to reveal the source of the bias effect at the interface and to regulate the interface magnetism.

Depending on the AFM material, FM/AFM films can be classified into three categories, including metal oxide films, metal films, and a third category of films such as sulfides, nitrides, fluorides, etc. [5,12,14–16]. The metal oxide films are more prominent in terms of pinning. As spintronics and magnetism develop, magnetite (Fe_3O_4) attracts the interest of many scientists with the characteristics of high spin polarization, high Curie temperature, and excellent resistivity suitability to semiconductors. Many different magnetic coupling mechanisms occur for the diverse defect structures such as antiphase boundaries [17,18], twin boundaries [19], etc. Fe_3O_4 is a FM material, which can be pinned by other AFM materials $BaFeO_3$, CoO, FeO, etc. [20–25]. Due to the intriguing magnetic properties and potential applications, a number of studies on Fe_3O_4/FeO core-shell or composite nanoparticles were carried out. For example, Swiatkowska-Warkocka *et al.* fabricated Fe_3O_4/FeO composite particles by pulsed laser deposition (PLD) and controlled the exchange bias by varying the laser energy [21]. Lak *et al.* fabricated monodisperse Fe_3O_4/FeO nanoparticles with different mean sizes and volume fractions of FeO synthesized via decomposition of iron oleate, and investigated the size effect on the

*These authors contributed equally to this work.
†Corresponding author: yxjiang11s@imr.ac.cn
‡Corresponding author: ttyao11s@imr.ac.cn

exchange bias energy and magnetic properties [26]. Estrader *et al.* investigated the correlation of magnetic properties of Fe_xO/Fe_3O_4 nanoparticles with different sizes and proposed an explanation for magnetic diffusion [27]. Phan *et al.* studied the exchange bias mechanism in the $Au/FeO/Fe_3O_4$ system [28]. However, due to lack of direct atomic-resolution imaging of the Fe_3O_4/FeO interface, the atomic structure, electronic properties, and magnetic coupling states at this interface remain almost unexplored.

In this work, to reveal the atomic origin of magnetic behaviors at FM/AFM interfaces, a combined study of scanning transmission electron microscopy (STEM) imaging, electron energy loss spectroscopy (EELS) and first-principles calculations is carried out to investigate the atomic and electronic structures and magnetic coupling at the Fe_3O_4/FeO heterointerfaces. The results will benefit the design and development of advanced magnetic and electronic devices.

II. EXPERIMENTAL AND COMPUTATIONAL METHODOLOGY

Single-crystalline FeO (001) substrate with purity of 99.99 wt % (Crystal Base Co., Ltd) was used for the fabrication of the Fe_3O_4/FeO (001) interface. TEM foils were prepared through procedures of cutting, mechanical grinding, dimpling, and Ar ion milling. The final Ar ion milling was conducted on a precision ion polishing system (Model 691, GATAN) with pressure of $\sim 1 \times 10^{-4}$ Pa whose accelerating gun voltage was set as 1–4 kV and incident beam angle as 4–5°. Although the ion milling was carried out at room temperature, the sample temperature during ion milling was estimated as ~100 °C due to the temperature rising effect by ion milling. Since the FeO is a metastable phase, a layer of Fe_3O_4 thin film was formed on the top and bottom surfaces of the FeO samples due to the oxidation of FeO during the ion milling [29–31]. ε-Fe_2O_3 films were used for the fabrication of the Fe_3O_4/FeO (111) interface. ε-Fe_2O_3 films were grown on $SrTiO_3$ (111) substrates by PLD using a commercial α-Fe_2O_3 target, a substrate temperature of 825 °C an oxygen pressure of 10 Pa, a laser beam frequency of 5 Hz, and a laser energy density of 1 J/cm^2. TEM specimens were fabricated through the above-mentioned procedures.

STEM observations were conducted by using 200-kV STEM (ARM 200FC, JEOL) and 300-kV STEM (Spectra 300, FEI) with pressure of 10^{-5} Pa in the specimen chamber. For STEM imaging, a probe size of ~1 Å and a probe convergence angle of ~25 mrad were adopted. The collection semiangles of detectors for high-angle annular dark field (HAADF) imaging were 68-280 mrad. Simulations of HAADF images were performed using the quantitative TEM/STEM simulations (QSTEM) based upon the multislice theory with frozen phonon modeling method [32,33]. For the HAADF image simulations, an acceleration voltage of 200 kV, a Cs of 0.01 mm, a source size of 0.12 nm, a probe convergence angle of 30 mrad, and a collection semiangle of 68−280 mrad were used. The Fe_3O_4/FeO supercell with a dimension of 22.69 Å × 22.69 Å × 26.66 Å was adopted for the image simulations. The assumed slice was 1.33 Å. EELS spectra of pure FeO were obtained using a crashed sample without Ar ion milling.

First-principles calculations based on density functional theory (DFT) [34,35] were carried out using the Vienna *Ab initio* Simulation Package (VASP) [36,37]. A generalized gradient approximation (GGA) in the form of the Perdew-Burke-Ernzerhof (PBE) [38] generalized function was employed. The projector augmented wave (PAW) [39,40] pseudopotential method was used, where the plane wave energy cutoff was 500 eV. The Fe $3d^6\,4s^2$ and O $2s^2\,2p^4$ were treated as valence states. The conventional GGA (PBE) method and the GGA + U method were compared, and the effective Hubbard parameter $U_{\text{eff}} = 3.8$ eV for Fe ions was finally chosen based on the available experimental results ($U_{\text{eff}} = U - J$). A ferromagnetic model and an antiferromagnetic model for Fe_3O_4/FeO (001) and a majority-spin model and a minority-spin model for Fe_3O_4/FeO (111) are considered. $\sqrt{2}a_1 \times \sqrt{2}a_1 \times a_1$ FeO cells ($a_1 = 4.3$ Å) and $a_2 \times a_2 \times a_2$ Fe_3O_4 cells ($a_2 = 8.4$ Å) were modeled in a 5:4 ratio for the Fe_3O_4/FeO (001) interface. The Fe_3O_4/FeO superlattice model was established to obtain the appropriate interface spacing by structural optimization, and then the slab model was established based on the obtained interface spacing to ensure that different interfaces can be calculated separately. For the structural optimization, all atomic Hellmann-Feynman forces were less than 30 meV/Å. $2 \times 2 \times 1$ and $6 \times 6 \times 1$ Monkhorst-Pack k point meshes [41] were used for type A and type B supercells. The surfaces of the slab models were fixed during the calculations.

III. RESULTS AND DISCUSSION

Epitaxial Fe_3O_4/FeO (001) samples were fabricated through an oxidation transformation of FeO during the Ar ion milling under a pressure of $\sim 1 \times 10^{-4}$ Pa (see details in the Methods section). The plane-view bright-field transmission electron microscopy (TEM) image of the sample is presented in Fig. 1(a), in which wrinkleslike contrast appears due to the formation of Fe_3O_4 on the surfaces of FeO. Figure 1(b) shows the corresponding composite selected area electron diffraction (SAED) pattern viewed along the $[001]_{FeO}$ axis, which is featured with double diffraction spots originated from moiré fringes. This SAED pattern indicates that Fe_3O_4 grows epitaxially on the FeO substrate with the orientation relationship of $[001](110)_{Fe_3O_4}//[001](010)_{FeO}$; the lattice matching relationship is 5:4. To further confirm the coexistence of Fe_3O_4 and FeO, EELS spectra were obtained. Fe-$L_{2,3}$ and O-K edges obtained from the pure FeO (blue, crashed sample) and the FeO sample with Fe_3O_4 (red, ion-milled sample) are shown in Figs. 1(c) and 1(d), respectively. As can be seen, the Fe-$L_{2,3}$ edge of the ion-milled FeO sample shifts toward the high-energy direction compared to that of pure FeO. It suggests that the valence state of Fe ions in the ion-milled FeO sample is higher than that of pure FeO, which is consistent with the formation of Fe_3O_4 due to the oxidation of FeO during Ar ion milling [42].

The switching of magnetic coupling states between Fe_3O_4 and FeO was investigated by the longitudinal magneto-optical Kerr effect (MOKE) with a laser diode (wavelength, 670 nm; beam diameter, ~0.2 mm). Figure 2 shows the Kerr microscope images of the Fe_3O_4/FeO (001) sample subjected to an external magnetic field of (a) 0 Oe, (b) 2550 Oe, and (c) −3000 Oe. Light and dark contrast correspond to the up

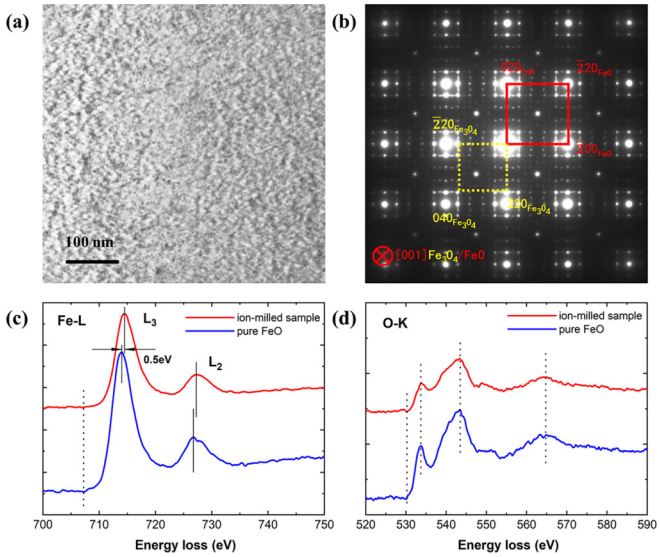

FIG. 1. TEM characterizations of FeO samples prepared by Ar ion milling. (a) Bright-field TEM image viewed along the [001] axis. (b) Corresponding composite SAED pattern of FeO and Fe_3O_4, indicating the orientation relationship of $[001](110)_{Fe_3O_4}//[001](010)_{FeO}$. (c) Fe-$L_{2,3}$ edges and (d) O-K edges obtained from the pure FeO (blue, crashed sample) and the FeO sample with Fe_3O_4 (red, ion-milled sample). The Fe-$L_{2,3}$ edge of the ion-milled sample shifts toward the high-energy region.

and down magnetizations, respectively. As can be seen, the magnetic domains change the direction of magnetic moments when applying positive and negative external magnetic fields. It suggests that the magnetic coupling states between Fe_3O_4 and FeO can be switched between ferromagnetic and antiferromagnetic couplings. However, it is still not clear which magnetic coupling is the intrinsic and energetically favorable one.

To reveal the atomic structure of heterointerfaces, it is sure that high-resolution observations from the cross-sectional direction are more direct and helpful. However, in this study, the Fe_3O_4 phase was formed due to the oxidation of FeO during the Ar ion milling of plane-view TEM samples. Thus, the Fe_3O_4 thin layers epitaxially grew on the up and bottom surfaces of the FeO TEM thin foils and the Fe_3O_4/FeO (001) interface was parallel to the surface of TEM thin foils. As a result, TEM observations of the Fe_3O_4/FeO (001) interface along the cross-sectional direction are difficult. Thus, atomic-resolved high-angle annular dark field (HAADF) images of the ion-milled Fe_3O_4/FeO sample were obtained from the plane-view direction, and the results were presented in Fig. 3. For better presentation, the HAADF images were colored. Clearly, there are square units with strong-weak contrast periodically appearing in the HAADF images due to the formation of moiré fringes. Based on the orientation relationship between Fe_3O_4 and FeO and the information of atomic structure conveyed by Fig. 3(a), several possible models of the Fe_3O_4/FeO (001) interface are built and relaxed by DFT calculations. Figures 3(d) and 3(e) show model I and model II of the Fe_3O_4/FeO (001) interface whose atomic structures cannot be distinguished from the top view direction. The simulated HAADF images using model I and model II are

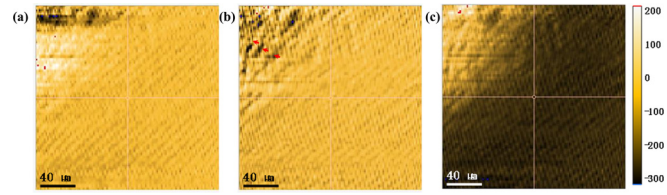

FIG. 2. Kerr microscope images of the Fe_3O_4/FeO sample subjected to external magnetic field of (a) 0 Oe, (b) 2550 Oe, and (c) −3000 Oe. The magnetic domains change the direction of magnetic moments when applying positive and negative external magnetic fields.

the same and are shown in Fig. 3(c). The simulated HAADF image matches well with the experimental ones [Figs. 3(a) and 3(b)]. It suggests that model I and model II are two possible and reasonable models for the Fe_3O_4/FeO (001) interface.

Epitaxial Fe_3O_4/FeO samples with another orientation relationship were fabricated through a reduction transformation of ε-Fe_2O_3 thin films (see details in the Methods section). Compared with previous studies [43], the present work clearly obtains the atomic-resolution STEM images and investigates the electronic structure and magnetic coupling at the interface. Figures 4(a) and 4(b) show the HAADF and annular bright field (ABF) images of the Fe_3O_4/FeO (111) interface. The orientation relationship between Fe_3O_4 and FeO is $[11\bar{2}](111)_{Fe_3O_4}//[11\bar{2}](111)_{FeO}$. The HAADF image can only present Fe atoms of iron oxides while the ABF image can present clearly both Fe and O atomic columns. An atomic model is inserted in the ABF image to better understand the interfacial structure. The interface is denoted by the arrows. It can be seen that the epitaxial growth between Fe_3O_4 and FeO is perfect and this interface is very flat.

The formation energies of both Fe_3O_4/FeO interfaces were calculated by the first-principles calculations. All superlattice model structures were first preprocessed with full relaxation to determine the interface spacing and the number of atomic layers affected by the interface. The results show that the length influenced by the interface is about 5 Å along the z axis (four atomic layers). Slab models were then reconstructed to calculate the interfaces separately. The four atomic layers at the surfaces of slab models were fixed during the calculations. For the Fe_3O_4/FeO (001) interface, the formation energy of model I is 10 eV lower than that of model II, and the interfacial formation energy differs by 470 mJ/m^2. So it can be determined that the stable configuration of Fe_3O_4/FeO is model I. For better determination of the magnetic coupling mechanism accompanying the interface, the electronic and atomic structures of the FM or AFM coupling heterogeneous interfaces were calculated separately. The energy of AFM coupling interface is just 34 mJ/m^2 lower than that of the FM one, which implies that the magnetic moment switching of Fe_3O_4 can be achieved under the action of small external fields.

The modulation of magnetic properties largely depends on the regulation of atomic and electronic structures, since any disturbance to the crystal structure in oxide magnetic systems may dramatically alter the properties such as conductivity and magnetic ordering. This is due to the fact that the local

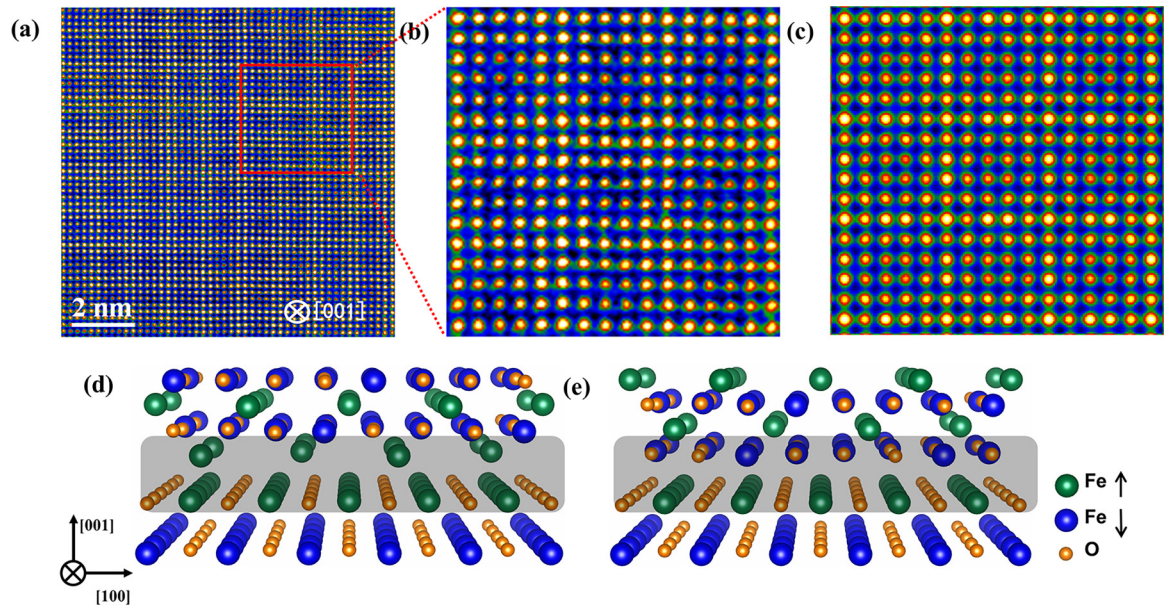

FIG. 3. HAADF images and atomic models the Fe_3O_4/FeO (001) interface. (a) Experimental HAADF images of the ion-milled Fe_3O_4/FeO sample obtained from the plane-view direction ([001] axis). (b) HAADF image showing the enlarged 3 × 3 superlattice from the red frame of (a). (c) Simulated HAADF images using model I and model II. (d), (e) Possible atomic models (model I and model II) of the Fe_3O_4/FeO interface. O atoms, spin-up, and spin-down Fe atoms are shown with yellow, green, and blue balls, respectively.

properties of electron hopping mechanisms and superexchange interactions strongly depend on the local atomic alignment and structures [44]. The two types of Fe_3O_4/FeO interfaces and the accompanying two different modes of magnetic coupling are further investigated. The density of states (DOS), local density of states (LDOS), and projected density of states (PDOS) are plotted. As shown in Fig. 5 for DOS and LDOS of the atomic layers at the Fe_3O_4/FeO (001) interface [shaded parts in Figs. 5(b) and 5(e)], the FM and AFM interfaces show almost the same electronic structures, which is the reason for the small value of the formation energy difference. Figures 5(a) and 5(d) show the DOS of the bulk Fe_3O_4 and bulk FeO, exhibiting semimetallic and AFM insulating properties, respectively. Figures 5(c) and 5(f) show LDOS of Fe atoms at the interface in Fe_3O_4 and Fe and O atoms at the FeO interface, plotted with red, green, and purple lines, respectively. It is noteworthy that Fe_3O_4 exhibits a metal-insulator transition in Figs. 5(c) and 5(f). The band gap of 0.34 eV at the interface is much smaller than the band gaps of 0.90 eV for Fe_3O_4 and 1.63 eV for FeO. No electronic states occupy the Fermi level, exhibiting insulating properties.

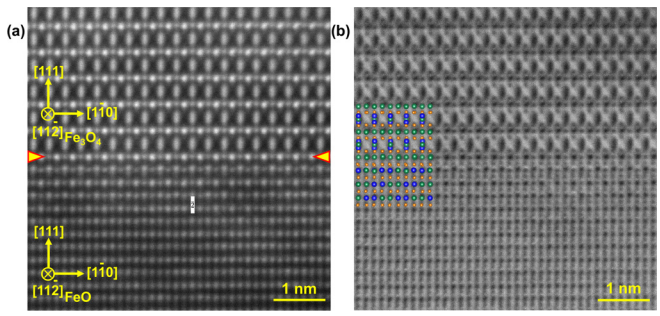

FIG. 4. HAADF and ABF images of the Fe_3O_4/FeO (111) interface obtained from the ε-Fe_2O_3 sample after two-step-reducing reaction. (a) Experimental HAADF image viewed along the [11$\bar{2}$] zone axis. (b) Corresponding ABF image with an inserted atomic model. The interface is denoted by the red arrows.

A large lattice distortion is observed at the Fe_3O_4/FeO (001) heterointerface, where FeO is subjected to in-plane tensile stress and Fe_3O_4 is subjected to in-plane compressive stress. Figure 6 presents the atomic structures and PDOS of Fe_3O_4 at the interface layer. Figures 6(a) and 6(b) show the atomic positions after relaxation at the AFM and FM interfaces respectively, producing atomic displacements and reduction in the atomic layer spacing compared to the initial model. Magnetic analysis reveals that the magnetic moments of Fe atoms in the Fe_3O_4 layer in the blue box are reduced. The magnetic moments of Fe atoms away from the interface layer are between $3.93\mu_B$ to $4.17\mu_B$ and $-4.07\mu_B$ to $-4.03\mu_B$, while those at the interfaces are $3.61\mu_B$ to $-3.66\mu_B$ and $-3.65\mu_B$ to $-3.56\mu_B$. The atomic spin directions at the interfaces remain unchanged and the magnetic moments are reduced by about 10%. Figures 6(c)–6(e) show the PDOS of the bulk Fe_3O_4, FM, and AFM interface of Fe_3O_4/FeO, respectively. Comparing the PDOS of bulk and the interfaces, we can see that partial d_{xz} and d_{yz} orbitals (green and red lines) at the interfaces shift from the conduction band to the valence band. It indicates that the electrons increase at the interface compared to the bulk Fe_3O_4, and d_{xz} and d_{yz} orbitals are preferentially occupied by the electrons, as shown with the black arrow. These results show that a large distortion at the interface makes the d_{xz} and d_{yz} orbitals of the interfacial Fe atoms preferentially occupied by the electrons, leading to the reduced valence state and magnetic moments of the interfacial Fe atoms, and therefore cause the metal-insulator transition.

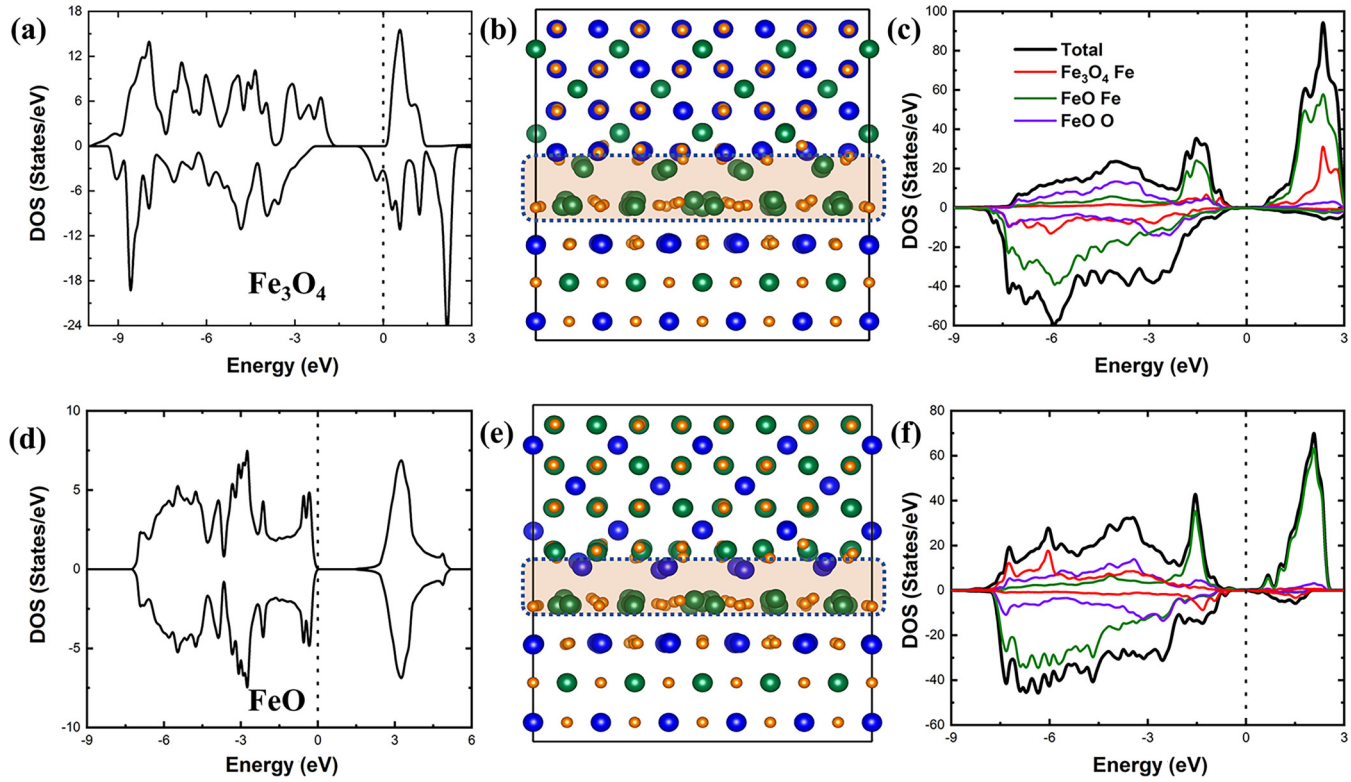

FIG. 5. DOS and LDOS of the atomic layers at the Fe_3O_4/FeO (001) interface. (a) DOS of Fe_3O_4 in bulk with semimetallic and (d) DOS of FeO in bulk with AFM insulating properties. (b), (e) FM and AFM model for interface in model I. (c), (f) DOS and LDOS at the FM and AFM interface (dashed line). Total DOS, PDOS of Fe in Fe_3O_4, PDOS of Fe and O in FeO are plotted with black, red, green, purple lines.

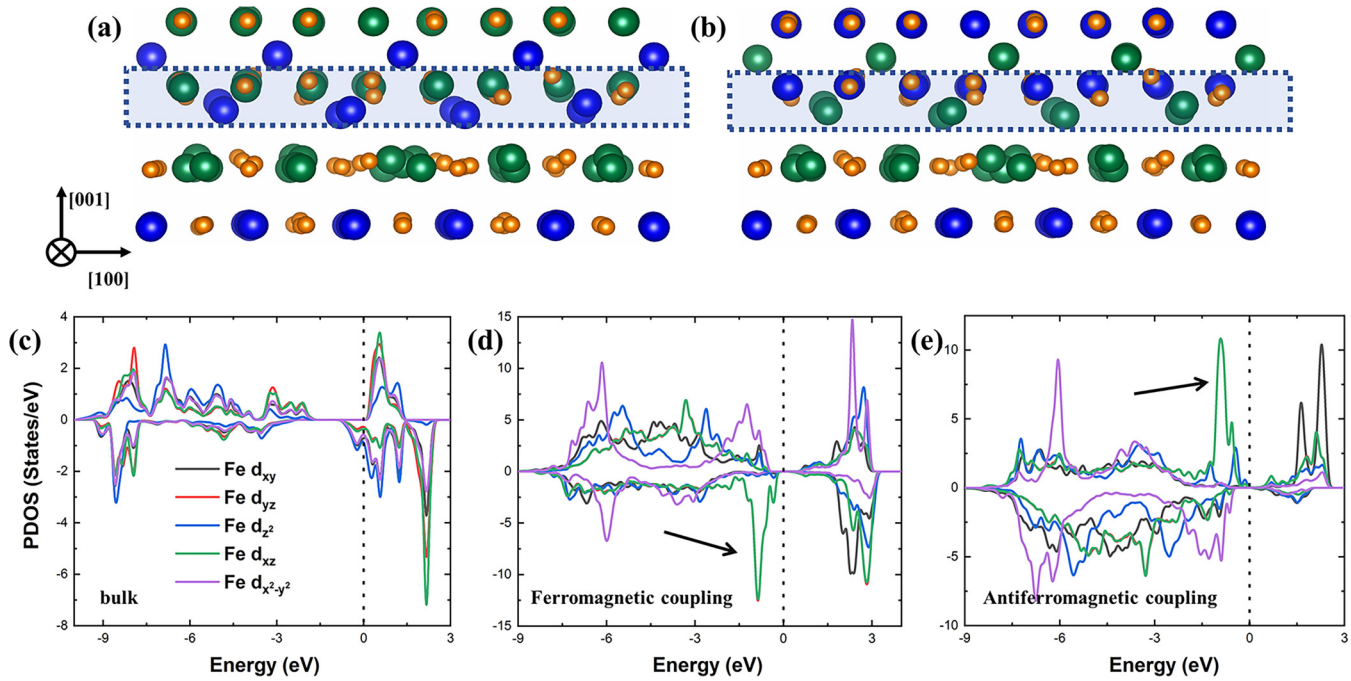

FIG. 6. Atomic structure and PDOS of the Fe_3O_4 layer at the Fe_3O_4/FeO (001) interface. (a), (b) The structures of the FM and AFM Fe_3O_4/FeO interface viewed along the [001] direction. The PDOS of the Fe atoms in the blue-dotted-line boxes are plotted. (c) PDOS of Fe in bulk Fe_3O_4 as reference. (d), (e) The PDOS of the FM and AFM interfaces. The preferentially occupied d_{yz}, d_{xz} orbitals are shown with the black arrows.

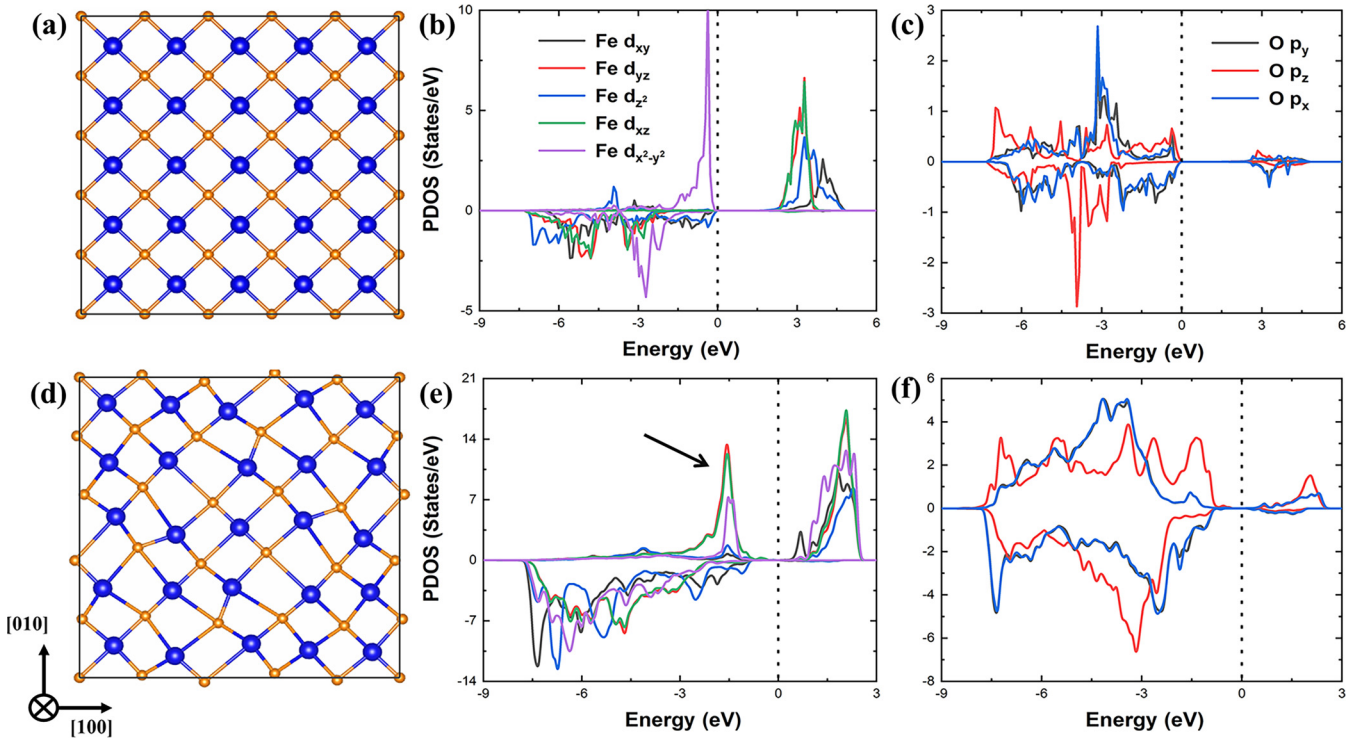

FIG. 7. Atomic structure and DOS of FeO. (a)–(c) Atomic structure and DOS of bulk FeO. (d), (e) Atomic structure and DOS of FeO at the Fe_3O_4/FeO (001) interface. (b),(e) PDOS of Fe d orbitals. The peaks of d_{xz}, d_{yz} appearing at the Fermi level originate from the cross-interface orbitals, shown with the black arrow. (c), (f) PDOS of p orbitals of O atoms. DOS at the interfaces have an overall shift to lower energy levels.

On the other hand, the atomic structure of FeO at the interface exhibits obvious lattice distortion, showing a jagged structure, as shown in Figs. 6(d) and 7(a). The corresponding PDOS of Fe and O atoms of a FeO atomic layer in the bulk and at the interface are shown in Figs. 7(b) and 7(c) and Figs. 7(e) and 7(f). The interfacial FeO layer still exhibits the insulating character like that in the bulk but the band gap decreases from 1.30 eV to 0.34 eV. Electrons near the Fermi level in the FeO bulk occupy $d_{x^2-y^2}$ orbitals, while at the interface the occupation in the $d_{x^2-y^2}$ orbitals observably reduces and the electrons emerge to occupy d_{yz} and d_{xz} orbitals, denoted by the black arrow in Fig. 7(e). This change corresponds to the preferentially occupied d_{xz} and d_{yz} orbitals of the interfacial Fe atoms in Fe_3O_4. The coupling between Fe_3O_4 and FeO across the interface is through the d_{yz} and d_{xz} orbitals. It reveals that the obvious lattice distortion splits partial $d_{x^2-y^2}$ orbitals of FeO to higher energy levels, resulting in the coupling between Fe_3O_4 and FeO across the interface through the preferentially occupied d_{yz} and d_{xz} orbitals.

For comparison with the Fe_3O_4/FeO (001) interface, the Fe_3O_4/FeO (111) interface is further explored by first-principles computations. Figures 8(a) and 8(d) show the majority-spin and minority-spin models of the Fe_3O_4/FeO (111) interface, which are defined by the spin of the Fe atoms of Fe_3O_4 at the interface. The interface is denoted by the red dashed line. The black box indicates the Fe_3O_4 and FeO in the interface layer. Figures 8(b) and 8(e) show the LDOS and Figs. 8(c) and 8(f) show the PDOS of Fe_3O_4 at the interface. The atomic distortion at this interface is much smaller compared to the Fe_3O_4/FeO (001) interface. The Fe atomic magnetic moment of the Fe_3O_4 interface layer is $3.7 - 4.1\mu_B$, similar to that of the away-from-interface layer, which is different from the reduced magnetic moment at the Fe_3O_4/FeO (001) interface. The band gap at the majority-spin interface of Fe_3O_4 and FeO is about 0.17 eV, and the electronic states at the Fermi energy level mainly originate from the d_{yz} and d_{xz} orbitals. Defect states appear at the minority-spin interface, which originates from the Fe atoms in FeO (Fig. 9), while the states of d_{yz} orbitals of Fe atoms in Fe_3O_4 at the Fermi energy level disappear. It can be concluded that the difference in the atomic structure of the two types of interfaces is small but the deference in the electronic structure is obvious.

Figures 9(b) and 9(c) show the PDOS of Fe atoms in FeO at the majority-spin and minority-spin interface. The d_{yz} and d_{xz} orbitals of Fe atoms in FeO at the top of the valence band and the bottom of the conduction band correspond to those in Fe_3O_4, indicating that the coupling between Fe_3O_4 and FeO across the Fe_3O_4/FeO (111) interface is also through the d_{yz} and d_{xz} orbitals. The defect states at the minority-spin interface mainly come from the d_{xy} orbitals, as shown in Fig. 9(c). In contrast, the corresponding d_{xy} orbitals appear at the top of the valence band at the majority-spin interface, as shown in Fig. 9(b). The d_{xy} orbitals have similar energies with those of the d_{yz} and d_{xz} orbitals at the majority-spin interface, while the d_{xy} orbitals at the minority-spin interface are shifted to higher energy levels. Thus the spin inversion of Fe_3O_4 at the Fe_3O_4/FeO (111) interface can induce orbital splitting in FeO, which is not found at the Fe_3O_4/FeO (001) interface, though the couplings across the two interfaces are both through the d_{yz} and d_{xz} orbitals. It can be seen that the effect of the coupling between FeO and Fe_3O_4 is closely related to the orientation of the interface.

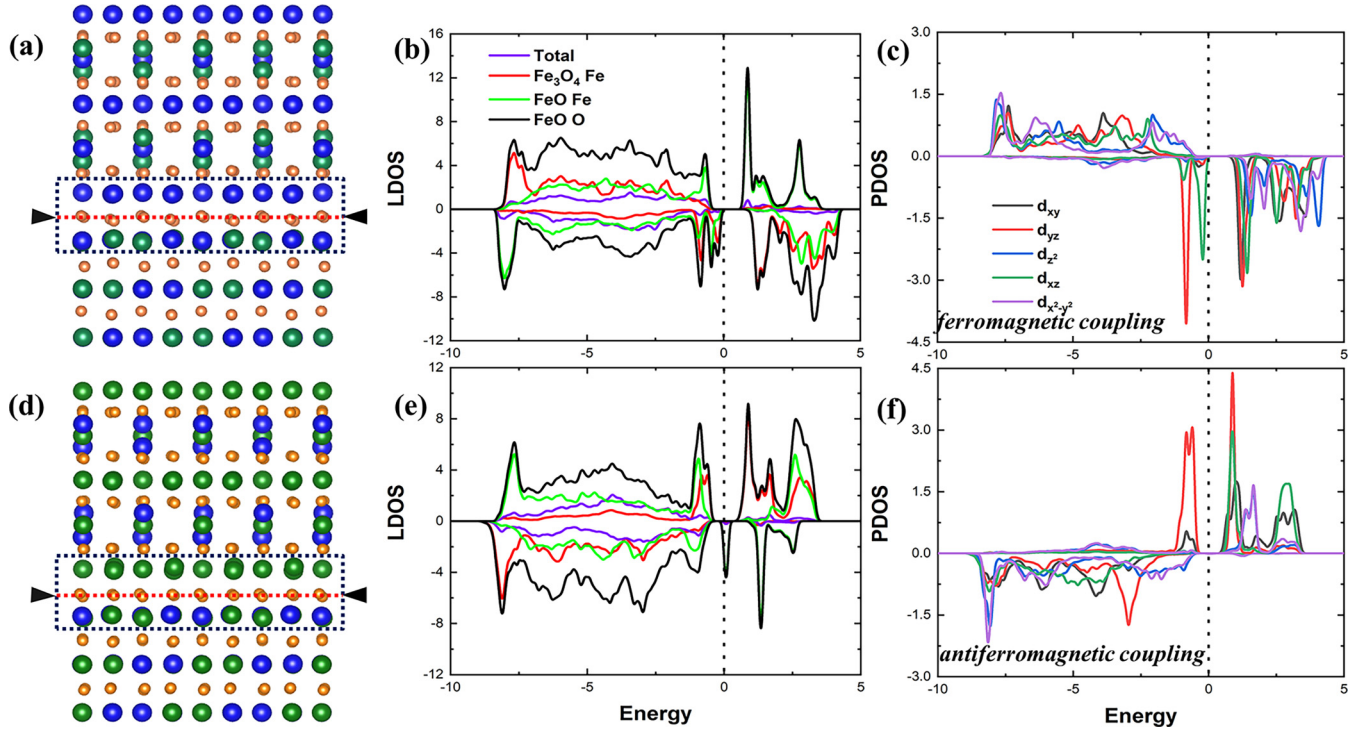

FIG. 8. Atomic structure and density of states at the Fe_3O_4/FeO (111) interface. (a), (d) Atomic models of majority-spin and minority-spin interfaces. The red dashed lines show the interfaces. The interfacial Fe atoms are denoted in the black box. (b), (e) LDOS at the majority-spin and minority-spin interfaces. (c), (f) PDOS of interfacial Fe atoms in Fe_3O_4.

IV. CONCLUSIONS

In this study, atomic and electronic structures of Fe_3O_4/FeO heterointerfaces with two orientation relationships are investigated by means of TEM and first-principles calculations. For the Fe_3O_4/FeO (001) interface, interesting moiré fringes were observed. The stress effect at the interface and the disruption of the crystal field cause a strong lattice distortion, leading to a metal-insulator transition in the Fe_3O_4 atomic layer at the interface. Due to the lattice distortion, the d_{xz} and d_{yz} orbitals of the interfacial Fe atoms are preferentially occupied by the electrons, which reduces the valence state and magnetic moments of the interfacial Fe atoms. For the Fe_3O_4/FeO (111) interface, the action of Fe in interfacial FeO on the Fe valence electrons in Fe_3O_4 leads to the appearance of defect energy levels at the AFM coupling interface, which induces a magnetic flip of Fe_3O_4. The AFM coupling at both types of Fe_3O_4/FeO interfaces is more stable than the FM coupling, but the energy difference between AFM and FM coupling is small. This feature of the Fe_3O_4/FeO interface will benefit its applications in low-power consumption magnetic and electronic devices.

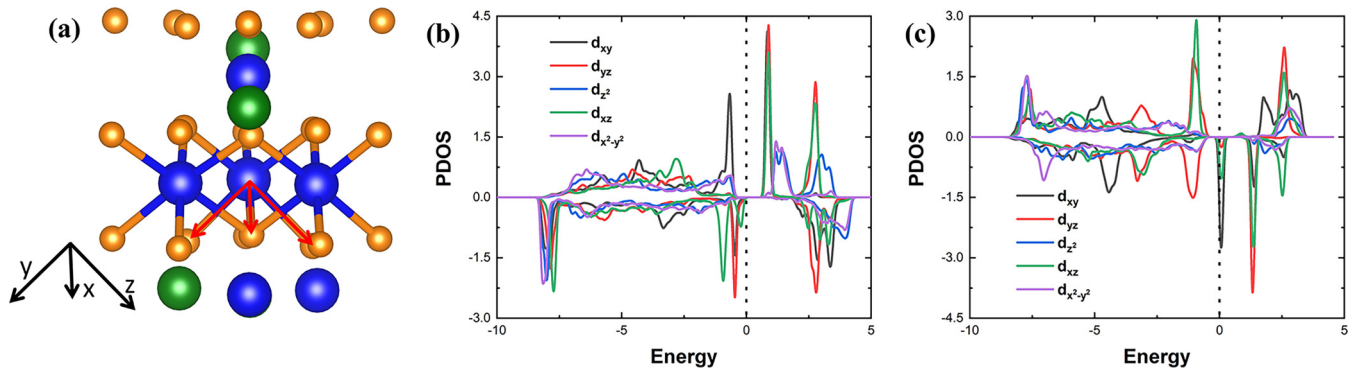

FIG. 9. Schematic of PDOS of the individual orbitals of Fe in FeO. (a) Modeling of the Fe_3O_4/FeO (111) interface. (b), (c) PDOS of Fe atoms in FeO in the majority-spin and minority-spin interfaces.

ACKNOWLEDGMENTS

We acknowledge support of this study by the National Natural Science Foundation of China (Grants No. 52271015 and No. 52001309), Jihua Laboratory (Project No. X210141TL210), and the Basic and Applied Basic Research Major Programme of Guangdong Province, China (Grant No. 2021B0301030003). The calculations were performed on TianHe-1(A) at the National Supercomputer Center in Tianjin.

[1] M. H. Kryder, Magneto-optic recording technology (invited), J. Appl. Phys. **57**, 3913 (1985).

[2] K. Shi, H. C. He, and N. Wang, Recent progress in application of multiferroic magnetoelectric materials on storage technology, J. Chin. Ceram. Soc. **39**, 1792 (2011).

[3] A. Segal, M. Karpovski, and A. Gerber, Sixteen-state magnetic memory based on the extraordinary Hall effect, J. Magn. Magn. Mater. **324**, 1557 (2012).

[4] H. Oezelt, A. Kovacs, F. Reichel, J. Fischbacher, S. Bance, M. Gusenbauer, C. Schubert, M. Albrecht, and T. Schrefl, Micromagnetic simulation of exchange coupled ferri-/ferromagnetic heterostructures, J. Magn. Magn. Mater. **381**, 28 (2015).

[5] J. Nogues and I. K. Schuller, Exchange bias, J. Magn. Magn. Mater. **192**, 203 (1999).

[6] C. Surgers, Electrical switching of the anomalous Hall effect, Nat. Electron. **1**, 154 (2018).

[7] S. Gangopadhyay, G. C. Hadjipanayis, C. M. Sorensen, and K. J. Klabunde, Magnetic properties of ultrafine Co particles, IEEE Trans. Magn. **28**, 3174 (1992).

[8] J. Sort, J. Nogués, S. Suriñach, J. S. Muñoz, M. D. Baró, E. Chappel, F. Dupont, and G. Chouteau, Coercivity and squareness enhancement in ball-milled hard magnetic-antiferromagnetic composites, Appl. Phys. Lett. **79**, 1142 (2001).

[9] W. H. Meiklejohn and C. P. Bean, New magnetic anisotropy, Phys. Rev. **105**, 904 (1957).

[10] W. H. Meiklejohn, Exchange anisotropy—a review, J. Appl. Phys. **33**, 1328 (1962).

[11] J. Nogués, J. Sort, V. Langlais, V. Skumryev, S. Suriñach, J. S. Muñoz, and M. D. Baró, Exchange bias in nanostructures, Phys. Rep. **422**, 65 (2008).

[12] M. Kiwi, Exchange bias theory, J. Magn. Magn. Mater. **234**, 584 (2001).

[13] M. A. Khan, J. Sun, B. D. Li, A. Przybysz, and J. Kosel, Magnetic sensors – A review and recent technologies, Mater. Res. Express **3**, 022005 (2021).

[14] S. Giri, M. Patra, and S. Majumdar, Exchange bias effect in alloys and compounds, J. Phys.: Condens. Matter **23**, 073201 (2011).

[15] F. Radu and Z. Hartmut, Exchange bias effect of ferro-/antiferromagnetic heterostructures, Springer Tracts Mod. Phys. **227**, 97 (2007).

[16] S. Giri and T. K. Nath, Exchange bias effect in nanostructured magnetic oxide, J. Nanosci. Nanotechnol. **14**, 1209 (2014).

[17] K. P. McKenna, F. Hofer, D. Gilks, V. K. Lazarov, C. L. Chen, Z. C. Wang, and Y. Ikuhara, Atomic-scale structure and properties of highly stable antiphase boundary defects in Fe_3O_4, Nat. Commun. **5**, 5740 (2014).

[18] C. Y. Gao, Y. X. Jiang, T. T. Yao, A. Tao, X. X. Yan, X. Li, C. L. Chen, X. L. Ma, and H. Q. Ye, Atomic origin of magnetic coupling of antiphase boundaries in magnetite thin films, J. Mater. Sci. Technol. **107**, 92 (2022).

[19] C. L. Chen, H. P. Li, T. Seki, D. Q. Yin, G. S. Santolino, K. Inoue, N. Shibata, and Y. Ikuhara, Direct determination of atomic structure and magnetic coupling of magnetite twin boundaries, ACS Nano **12**, 2662 (2018).

[20] Y. Ijiri, J. A. Borchers, R. W. Erwin, S. H. Lee, P. J. van der Zaag, and R. M. Wolf, Role of the antiferromagnet in exchange-biased Fe_3O_4/CoO superlattices, J. Appl. Phys. **83**, 6882 (1998).

[21] Z. W. Zaneta, K. Kenji, W. H. Qiang, K. Yukiko, and K. Naoto, Controlling exchange bias in Fe_3O_4/FeO composite particles prepared by pulsed laser irradiation, Nanoscale Res. Lett. **6**, 226 (2011).

[22] T. L. Qu, Y. G. Zhao, P. Yu, H. C. Zhao, S. Zhang, and L. F. Yang, Exchange bias effects in epitaxial Fe_3O_4/$BiFeO_3$ heterostructures, Appl. Phys. Lett. **100**, 242410 (2012).

[23] B. Leszczyński, G. C. Hadjipanayis, A. A. El-Gendy, K. Załęski, Z. Śniadecki, A. Musiał, M. Jarek, S. Jurga, and A. Skumiel, The influence of oxidation process on exchange bias in egg-shaped FeO/Fe_3O_4 core/shell nanoparticles, J. Magn. Magn. Mater. **416**, 269 (2016).

[24] S. G. Bhat and P. S. A. Kumar, Defect mediated exchange bias in oriented (111) Fe_3O_4/(100) GaAs, Thin Solid Films **621**, 26 (2017).

[25] P. Wang, C. Jin, X. Pang, W. C. Zheng, G. Q. Gao, D. S. Wang, D. X. Zheng, H. T. Dai, and H. L. Bai, Interfacial reconstruction, exchange bias and photocurrent effect in epitaxial Fe_3O_4/Co_3O_4 spinel heterostructure, Appl. Surf. Sci. **493**, 1236 (2019).

[26] A. Lak, M. Kraken, F. Ludwig, A. Kornowski, D. Eberbeck, S. Sievers, F. J. Litterst, H. Weller, and M. Schilling, Size dependent structural and magnetic properties of FeO-Fe_3O_4 nanoparticles, Nanoscale **5**, 12286 (2013).

[27] M. Estrader, A. L. Ortega, I. V. Golosovsky, S. Estradé, A. G. Roca, G. S. Alvarez, L. L. Conesa, D. Tobia, E. Winkler, J. D. Ardisson, W. A. A. Macedo, A. Morphis, M. Vasilakaki, K. N. Trohidou, A. Gukasov, I. Mirebeau, O. L. Makarova, R. D. D. Zysler, F. Peiró, M. D. Baró *et al.*, Origin of the large dispersion of magnetic properties in nanostructured oxides: Fe_xO/Fe_3O_4 nanoparticles as a case study, Nanoscale **7**, 3002 (2015).

[28] M.-H. Phan, J. Alonso, H. Khurshid, P. Lampen-Kelley, S. Chandra, K. S. Repa, Z. Nemati, R. Das, Ó. Iglesias, and H. Srikanth, Exchange bias effects in iron oxide-based nanoparticle systems, Nanomater. **6**, 221 (2016).

[29] J. P. McCaffrey, M. W. Phaneuf, and L. D. Madsen, Surface damage formation during ion-beam thinning of samples for transmission electron microscopy, Ultramicroscopy **87**, 97 (2001).

[30] K. H. Kim, D. A. Payne, and J. M. Zuo, Ion-beam induced domain structure in piezoelectric PMN-PT single crystal, Appl. Phys. Lett. **97**, 261910 (2010).

[31] S. C. Liou and W. A. Chiou, TEM study of microstructure of 316L stainless steel with different specimen preparation techniques, Microsc. Microanal. **22**, 2002 (2016).

[32] C. Koch and J. M. Zuo, Comparison of multislice computer programs for electron scattering simulations and the bloch wave method, Microsc. Microanal. **6**, 126 (2000).

[33] J. Woo, A. Borisevich, C. Koch, and V. V. Guliants, Quantitative analysis of HAADF–STEM images of MoVTeTaO M1 phase catalyst for propane ammoxidation to acrylonitrile, Chem. Cat. Chem. **7**, 3731 (2015).

[34] P. Hohenberg and W. Kohn, Inhomogeneous electron gas, Phys. Rev. **136**, B864 (1964).

[35] W. Kohn and L. J. Sham, Self-consistent equations including exchange and correlation effects, Phys. Rev. **140**, A1133 (1965).

[36] G. Kresse and J. Hafner, *Ab initio* molecular dynamics for liquid metals, Phys. Rev. B **47**, 558 (1993).

[37] G. Kresse and J. Furthmüller, Efficient iterative schemes for ab initio total-energy calculations using a plane-wave basis set, Phys. Rev. B **54**, 11169 (1996).

[38] J. P. Perdew, K. Burke, and M. Ernzerhof, Generalized gradient approximation made simple, Phys. Rev. Lett. **77**, 3865 (1996).

[39] P. E. Blöchl, Projector augmented-wave method, Phys. Rev. B **50**, 17953 (1994).

[40] G. Kresse and D. Joubert, From ultrasoft pseudopotentials to the projector augmented-wave method, Phys. Rev. B **59**, 1758 (1999).

[41] H. J. Monkhorst and J. D. Pack, Special points for Brillouin-zone integrations, Phys. Rev. B **13**, 5188 (1976).

[42] A. Tao, T. T. Yao, Y. X. Jiang, L. X. Yang, X. X. Yan, H. Ohta, Y. Ikuhara, C. L. Chen, H. Q. Ye, and X. M. Ye, Single-dislocation schottky diodes, Nano Lett. **21**, 5586 (2021).

[43] S. Meng, H. Zheng, S. F. Jia, L. Li, L. G. Zhao, R. H. Jiang, L. H. Ma, W. W. Meng, S. Z. Pu, D. S. Zhao, and J. B. Wang, Irradiation and size effects on redox reaction mechanisms in iron oxides, Chem. Mater. **33**, 1860 (2021).

[44] D. Gilks, Z. Nedelkoski, L. Lari, B. Kuerbanjiang, K. Matsuzaki, T. Susaki, D. Kepaptsoglou, Q. Ramasse, R. Evans, K. McKenna, and V. K. Lazarov, Atomic and electronic structure of twin growth defects in magnetite, Sci. Rep. **6**, 20943 (2016).